Stability Analysis of Grid-Forming Converters under dc-side Current Limitation in Primary Frequency Response Regime

Sayan Samanta, *Student Member, IEEE* and Nilanjan Ray Chaudhuri, *Senior Member, IEEE*

***Abstract*—The Stability of grid-forming converters (GFCs) interfacing renewable resources in a power system with multiple synchronous generators (SGs) is studied in the context of primary frequency response. The GFCs are divided into two classes based on the control methods – class-A: droop control, dispatchable virtual oscillator control (dVOC), and virtual synchronous machine (VSM); and class-B: matching control. First, averaged phasor models of these GFC classes are developed, which can be seamlessly integrated with positive sequence fundamental frequency planning models. Next, simplified averaged models are derived to study the stability of the dc-link voltage of the GFCs under dc-side current limitation in a generic multimachine system during primary frequency response. To that end, sufficiency conditions for stability of both classes and that of instability for class-A GFCs are established. Finally, the proposed stability conditions are verified using detailed switched models of two small systems and phasor models of a 4-machine and a 16-machine IEEE benchmark systems.**

***Index Terms*—Grid-forming converter, droop, virtual oscillator, virtual synchronous machine, matching control, Lyapunov stability, input-to-state stability, input-output stability**

NOMENCLATURE

Subscripts g, c, τ_g are used for SG, GFC and turbine governor and superscript * is used for reference quantities.

ω	angular frequency/speed
$v_{dc},\ i_{dc}$	dc-link voltage and dc-side source current
i_{dc}^{max}	maximum limit of the dc-side current
τ_c	equivalent delay representation in dc current source
G_c	conductance to represent dc-side losses
C_c	GFC dc-bus capacitance
$L,\ C,\ R$	GFC filter inductance capacitance and resistance
L_t, R_t	transformer inductance and resistance
i_x	dc-side current entering the GFC
$v_{tdq},\ i_{tdq}$	$d-q$ axes voltage and current at GFC terminal
$v_{dq},\ i_{dq}$	$d-q$ axes voltage and current at filter capacitor terminal
v_{cdq}	$d-q$ axis voltage at the transformer terminal connected to grid
m_{tdq}	modulation index for GFC in $d-q$ frame
d_{pc}	droop gain for class-A GFC
k_m	matching control gain for class-B GFC
k_c	dc voltage droop coefficient
$k_{p,ac},\ k_{i,ac}$	proportional and integral controller parameters for inner ac current control
$P,\ P_L$	real power output and load
θ	bus voltage angle
d_{pg}	SG inverse governor droop
k_d	SG damping torque coefficient
H_g	SG inertia constant
τ_g	SG turbine time constant

For the wind plant model:

ω_{wf}	wind turbine rotor angular speed
H_{wf}	wind turbine rotor inertia
$P_{wf}^m,\ P_{wf}^e$	mechanical and electrical power of the wind farm
P^{max}	maximum power point of the wind plant
c_p	power coefficient for wind turbine
$v_{wind},\ \rho$	wind speed and air density
A	turbine swept area.
β_1	turbine blade pitch angle.
θ_{PLL}	angle output of the PLL used in stator-side converter of the wind farm
$I_{d,ref},\ I_{q,ref}$	d and q axis current reference of the current controller of stator-side converter

This work was supported by NSF under grant award ECCS 1656983.

Sayan Samanta and Nilanjan Ray Chaudhuri are with The School of Electrical Engineering & Computer Science, The Pennsylvania State University, University Park, PA 16802, USA. sps6260@psu.edu, nuc88@psu.edu

I. INTRODUCTION

As converter-interfaced generation (CIG) is experiencing significant growth, the existing synchronous generator (SG)-dominated power system is now slowly progressing towards a combination of SGs and CIGs. Several studies are already reported in the literature including [1], [2] that focus on the impact of CIGs on bulk power systems with progressively declining inertia. However, since the CIGs are typically based on a grid-following strategy, most of these studies have considered this technology. Moreover, such studies involving time- and frequency-domain analyses, while very important, are mostly numerical in nature, and as a result, generic conclusions are hard to derive from them. In a recent work [3], the authors pointed out such deficiencies of the existing literature and summarized the major challenges of such low inertia systems. Out of these challenges, one important area is primary frequency response following loss of generation – especially in presence of grid-forming converters (GFCs), which is less understood compared to its grid-following counterpart. In this

work, we consider the bulk power system consisting SGs and GFCs and focus on the stability analysis of GFCs contributing towards primary frequency response.

GFC-interfaced renewable resources in future grids are expected to provide primary frequency support, so that underfrequency load shedding (UFLS) is averted. There are two classes of GFCs depending on the control philosophy: (A) either of droop, dispatchable virtual oscillator control (dVOC), and virtual synchronous machine (VSM); and (B) matching control [4]–[7] – we call the first group 'class-A' and the second group 'class-B' [8].

Reference [9] reported dc-link voltage instability in class-A GFCs when the dc-side and ac current limits are hit in the process of providing frequency support. On the other hand, class-B GFCs are shown to demonstrate a certain degree of superiority in this regard. In this work, the authors provided qualitative reasoning-based analysis for the dc-link voltage stability of GFC under different control strategies and instability of class-A GFC in presence of large load changes. However, analytical treatment of stability guarantees in presence of dc-side current limitations was reserved for future research.

Some of the recent works on the topic of stability analysis of power systems in presence of GFCs include [10], [11], and [12]. Reference [10] has focused on the small-signal stability of low inertia power systems in presence of GFCs and grid-following converters. As a result, dc-link voltage instability due to the presence of current limits was not considered. Authors in [11] proposed a dc-side voltage feedback strategy for class-A GFCs to address the instability problem. However, the authors did not present any analytical stability guarantees. In [12], the authors proposed a hybrid angle control approach to ensure almost global stability of Class-B GFCs using a novel nonlinear angle feedback control in presence of ac current limits. To the best of our understanding, this work did not consider dc-side current limitation, and restricted its analysis to a single GFC.

In [8] we proposed sufficiency conditions for stability of GFCs under dc-side current limitation, which were verified in a 2-bus system. In this paper, we extend our previous work and present a more detailed treatment of averaged modeling of GFCs that can be integrated with traditional multimachine planning models in the phasor framework. Next, reduced-order models of the multimachine systems with GFCs are derived. The validation and limitations of this reduced-order model are presented in detail. Further details of the dc-side source model and the impact of the selection of the dc-side current limitation are provided using the model of a Type-4 wind plant. These models are then used to study the Lyapunov stability and sufficiency conditions for stability and instability of different classes of GFCs. Finally, the accuracy of the proposed stability conditions is extensively tested on EMT models of an isolated GFC and the IEEE 9-bus system in addition to averaged phasor models of IEEE 4-machine and 16-machine systems.

II. Modeling and Control of GFCs

The typical circuit model of a GFC interfacing renewable resources is shown in Fig. 1 whose dc bus is connected for example, to the dc side of the ac-dc converter of a Type-4 wind turbine. We restrict our focus to the dc to ac unidirectional power flow scenario, i.e. energy storage is excluded from our analysis. The converter is operating at an 'off' maximum power point (MPP) to provide frequency support. Also, it is assumed that the converter ac current is within the allowable limit during primary frequency response.

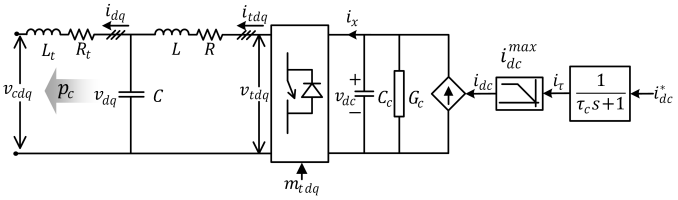

Fig. 1. Circuit model of GFC: dc-side current limit reflecting capacity of the renewable resource.

A. Modeling of GFCs Connected to Power Grid

We integrate a space-phasor model of GFCs with the traditional positive sequence fundamental frequency phasor model of the power grid for system planning. To that end, the components of the power system are divided into four categories – (a) SGs, (b) loads, (c) network, and (d) GFCs, as shown in Fig. 2. Reference [13] performed modeling adequacy study of such systems for capturing frequency dynamics and demonstrated that an algebraic network model is acceptable, which is followed here. The model of each component in the power system is mentioned next.

(a) A sixth-order subtransient model of SGs in their individual $d-q$ reference frames (rotating at ω_{gi} for ith SG) along with their exciters and turbine-governors [14] is used.
(b) Unless otherwise stated, the loads are represented with constant power models.
(c) An algebraic network model is used, which is interfaced with all the SGs, loads, and GFCs in the system. It solves the equation $I_{bus} = Y_{bus}V_{bus}$ in a synchronously rotating reference frame (rotating at ω^*) to calculate the voltages at each bus.
(d) The GFCs are also modeled in their respective $d-q$ reference frames rotating at speed ω_{ci} for the ith converter.

Next, the modeling of GFCs is discussed in details.

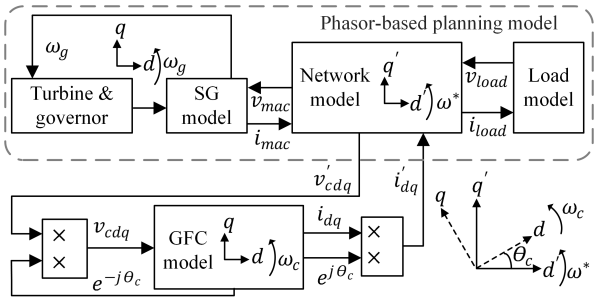

Fig. 2. GFC integrated with thr phasor model of the power system.

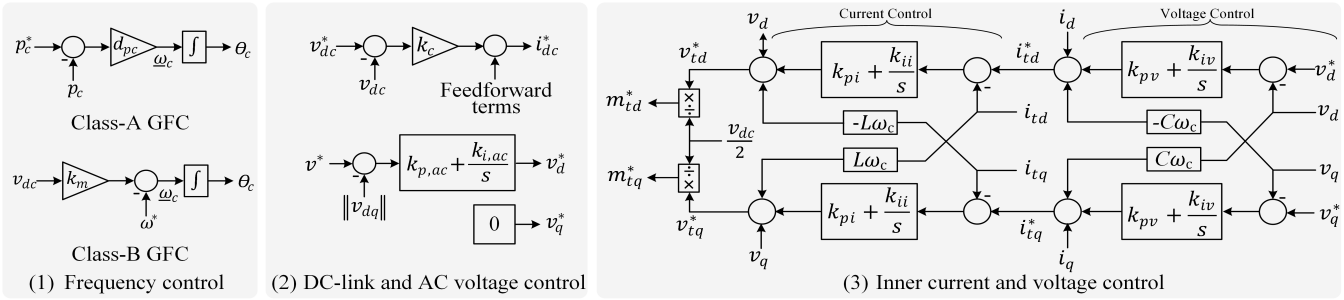

Fig. 3. Controls of GFCs: only frequency controls are different for two classes of GFCs.

The GFC shown in Fig. 1 is modeled using the following differential and algebraic equations,

$$\dot{i}_\tau = \frac{1}{\tau_c}\left(i_{dc}^* - i_\tau\right) \tag{1a}$$

$$\dot{v}_{dc} = \frac{1}{C_c}\left(i_{dc}^{max} sat\left(\frac{i_\tau}{i_{dc}^{max}}\right) - i_x - G_c v_{dc}\right) \tag{1b}$$

$$\begin{bmatrix}\dot{i}_{td}\\ \dot{i}_{tq}\end{bmatrix} = \begin{bmatrix}\frac{-R}{L} & \omega_c\\ -\omega_c & \frac{-R}{L}\end{bmatrix}\begin{bmatrix}i_{td}\\ i_{tq}\end{bmatrix} + \frac{1}{L}\begin{bmatrix}v_{td}-v_d\\ v_{tq}-v_q\end{bmatrix} \tag{1c}$$

$$\begin{bmatrix}\dot{v}_d\\ \dot{v}_q\end{bmatrix} = \begin{bmatrix}0 & \omega_c\\ -\omega_c & 0\end{bmatrix}\begin{bmatrix}v_d\\ v_q\end{bmatrix} + \frac{1}{C}\begin{bmatrix}i_{td}-i_d\\ i_{tq}-i_q\end{bmatrix} \tag{1d}$$

$$\begin{bmatrix}\dot{i}_d\\ \dot{i}_q\end{bmatrix} = \begin{bmatrix}\frac{-R_t}{L_t} & \omega_c\\ -\omega_c & \frac{-R_t}{L_t}\end{bmatrix}\begin{bmatrix}i_d\\ i_q\end{bmatrix} + \frac{1}{L_t}\begin{bmatrix}v_d-v_{cd}\\ v_q-v_{cq}\end{bmatrix} \tag{1e}$$

$$v_{td} = \frac{m_{td}v_{dc}}{2}, v_{tq} = \frac{m_{tq}v_{dc}}{2} \tag{1f}$$

Here, i_{dc}^{max} is the dc-side current limit reflecting the capacity of the renewable resource (see section IV-B for more discussion choice of i_{dc}^{max}); and $sat(y) = \begin{cases} y, \ if \ |y| \le 1 \\ sgn(y), \ if \ |y| > 1 \end{cases}$. In Fig. 1, $i_{dq} = i_d + ji_q$, $i_{tdq} = i_{td} + ji_{tq}$, $v_{dq} = v_d + jv_q$, $v_{cdq} = v_{cd} + jv_{cq}$, $m_{tdq} = m_{td} + jm_{tq}$.

To interface the GFC with the phasor model of the grid, the following steps are taken. The pcc voltage $v_{cdq}^{'}$ in network reference frame is first transformed to v_{cdq} in GFC's reference frame, which in turn is used in (1e). The GFC controller regulates voltage v_{dq} across the filter capacitor. Finally, current i_{dq} from (1d), (1e) in GFC reference frame is transformed back to network reference frame as $i_{dq}^{'}$ and used in solving the network equation as shown in Fig. 2. The coordinate transformation involves the term $e^{\pm j\theta_c}$, where θ_c is generated based on the type of GFC controls, i.e. class-A or class-B as described in the following section.

B. Control of GFCs

We follow the control laws described in [9], which are summarized here for completeness. The control of a GFC can be divided into three parts – (a) frequency control, (b) dc-link and ac-side voltage magnitude control, and (c) inner current and voltage control. Throughout the paper, symbols with $*$ as a superscript denote reference quantities.

1) Frequency control: The control of frequency of ac voltage imposed by the GFC differs among the two classes (see, Fig. 3-(1)) as discussed below.

Class-A GFC: For droop control the frequency is decided by the active power output p_c of the converter as shown in (2), where d_{pc} is the droop gain.

$$\underline{\omega}_c = \omega_c - \omega^* = d_{pc}\left(p_c^* - p_c\right), \quad p_c = \frac{3}{2}\left(v_d i_d + v_q i_q\right) \tag{2}$$

This mechanism is analogous in VSM and dVOC [5], [6].

Class-B GFC: For matching control, the frequency of the converter is proportional to v_{dc},

$$\omega_c = k_m v_{dc} \tag{3}$$

where, $k_m = \frac{\omega^*}{v_{dc}^*}$ is the matching control gain.

The angle reference θ_c mentioned earlier is generated as,

$$\theta_c = \theta_{c0} + \int_0^t \underline{\omega}_c d\tau \tag{4}$$

The remaining controllers are common for both classes of GFCs.

2) DC-link and ac-side voltage magnitude control: The dc-link voltage is regulated through $v_{dc} - i_{dc}$ droop control accompanied by feedforward compensation (the feedforward is applied for class-B GFC as in [9]) to determine the dc-side current reference i_{dc}^*,

$$i_{dc}^* = k_c(v_{dc}^* - v_{dc}) + \frac{p_c^*}{v_{dc}^*} + G_c v_{dc} + \frac{v_{dc}i_x - p_c}{v_{dc}^*} \tag{5}$$

where, k_c is the dc-link voltage droop coefficient. This $v_{dc} - i_{dc}$ droop control has been explained in the context of a Type-4 wind turbine in section IV-B where the wind generator stator-side converter is responsible for this.

The ac voltage magnitude is regulated by a PI controller,

$$v_d^* = k_{p,ac}\underline{v}_d + k_{i,ac}\int_0^t \underline{v}_d(\tau)d\tau, \quad v_q^* = 0 \tag{6}$$

where, $\underline{v}_d = \left(v^* - \left\|v_{dq}\right\|\right)$, and $k_{p,ac}$ and $k_{i,ac}$ are the proportional and integral control parameters, respectively. Figure 3-(2) shows the above-mentioned controllers.

3) Inner control loops: Figure 3-(3) shows the inner loops consisting of ac voltage and current control, which are designed in the converter's individual $d-q$ reference frame whose angular frequency ω_c is generated as described earlier.

III. Reduced-order Model for Stability Analysis

We derive the reduced-order model of a generic test system with m_1 SGs, n_1 GFCs and p_1 load buses from its detailed model described above. The model should be suitable for

stability analysis of v_{dc} in presence of dc-side current limits within the primary frequency response regime, i.e. after a generation loss or large increase in load. It was observed in [9] that during such events, the increase in P_c may lead to dc-side current limit hitting, which affects the stability of v_{dc}.

To derive the model, we make the following assumptions: (1) the inner current and voltage control loops shown in Fig. 3-(3) track the references instantaneously, (2) the dc-link model of the GFC and the swing equation of the SG along with corresponding turbine-governor equations can represent frequency dynamics, (3) SGs are rated to deliver any load change in the system, (4) time constant τ_c of the dc energy source is neglected, and (5) a dc power flow model is assumed to be adequate for the system.

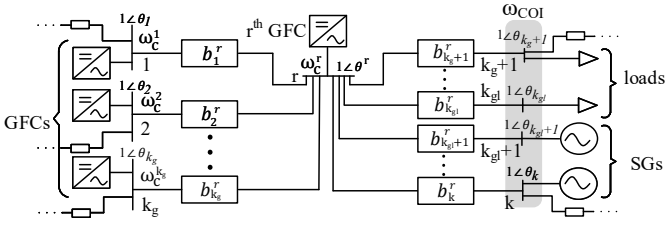

Fig. 4. Single line diagram of the connectivity of the r^{th} GFC to its neighboring buses in a generic case. Superscript r on k_g, k_{gl}, and k are not shown to avoid clutter.

A. Reduced-order Model of Class-A GFCs

For any r^{th} class-A GFC, let us assume that it is connected to k^r no. of neighboring buses as shown in Fig. 4. Out of those k^r buses, other GFCs are connected to k_g^r buses, no GFCs or SGs are connected to $k_{gl}^r - k_g^r$ buses, and SGs are connected to the remaining buses. The GFCs and SGs may or may not have local loads, but no GFC and SG are connected to the same bus. We define $\mathcal{N}(r)$ as the immediate neighborhood of the node corresponding to the rth GFC in a graph where other GFCs are connected, implying $|\mathcal{N}(r)| = k_g^r$. The angular frequency imposed by the droop control of the ith GFC at bus i is ω_c^i, $\forall i \in r \cup \mathcal{N}(r)$, while the angular frequencies of the rest of the neighboring buses are assumed to be the Center of Inertia (COI) frequency ω_{COI}. This is a good approximation, since electromechanical oscillations of individual generators are not of interest – rather the inertia-weighted average is under consideration, see for example [15]. The reduced-order model can be written as,

$$\dot{P}_{cg}^r = b^r\left(d_{pc}^r\left(P_c^{r*} - P_c^r\right) + \omega^*\right) - b_g^r\left(\underline{\omega}_{COI} + \omega^*\right) - \sum_{i\in\mathcal{N}(r)} b_i^r\left(d_{pc}^i\left(P_c^{i*} - P_c^i\right) + \omega^*\right) \quad (7a)$$

$$\dot{\underline{\omega}}_{COI} = \frac{1}{2H_T}\left[P_{\tau gT} - P_{gT} - k_{dT}\underline{\omega}_{COI}\right] = \frac{1}{2H_T}\left[P_{\tau gT} + P_{cT} - P_{LT} - k_{dT}\underline{\omega}_{COI}\right] \quad (7b)$$

$$\dot{P}_{\tau gT} = \frac{1}{\tau_{gT}}\left[P_{gT}^* - d_{pgT}\underline{\omega}_{COI} - P_{\tau gT}\right] \quad (7c)$$

$$\dot{v}_{dc}^r = \frac{1}{C_c^r}\left[-G_c^r v_{dc}^r + i_{dc}^{max,r}\, sat\left(\frac{k_c^r\left(v_{dc}^{r*} - v_{dc}^r\right)}{i_{dc}^{max,r}}\right) - \frac{P_c^r}{v_{dc}^r}\right], \quad r = 1,\ldots,n_1 \quad (7d)$$

We introduce the following notations pertaining to the rth GFC bus and neighboring buses shown in Fig. 4: b_i^r denotes admittance of the branch connecting the bus of the rth GFC and bus i, $\phi_i^r = \theta^r - \theta_i$; $P_{cg}^r = \sum_{i=1}^{k^r} b_i^r \phi_i^r$; $P_c^r = P_{cg}^r + P_L^r$; $P_{cT} = \sum_{r=1}^{n_1} P_c^r$; $b^r = \sum_{i=1}^{k^r} b_i^r$; $b_g^r = \sum_{i=k_g^r+1}^{k^r} b_i^r$; whereas the rest are independent of the location of the rth GFC: $H_T = \sum_{i=1}^{m_1} H_g^i$; $d_{pgT} = \sum_{i=1}^{m_1} d_{pg}^i$; $\tau_{gT} = \tau_g^i\ \forall i$, $\underline{\omega}_g^i = \omega_g^i - \omega^*$, $\underline{\omega}_{COI} = \frac{1}{H_T}\sum_{i=1}^{m_1} H_g^i \underline{\omega}_g^i$, $P_{\tau gT} = \sum_{r=1}^{m_1} P_{\tau g}^r$, $P_{gT}^* = \sum_{r=1}^{m_1} P_g^{r*}$, $k_{dT} = \sum_{i=1}^{m_1} k_d^i$ – superscript i denotes ith generator; $P_{LT} = \sum_{j=1}^{n_1+m_1+p_1} P_{Lj}$ with P_{Lj} denoting the load in jth bus.

B. Model for Stability Analysis of Class-A GFCs

The class-A GFC acts as a buffer to adjust the frequency of its terminal voltage in order to deliver the power P_c demanded by the system, which in turn affects the dc-link voltage dynamics. The converter has no direct control over P_c and the dc-link dynamics does not have any 'feedback mechanism' to alter it. Therefore, the stability of the dc-link voltage of class-A GFCs described by (7d) can be analyzed in isolation. Let, $v_{dc}^r = y > 0$, $v_{dc}^{r*} = y^*$, $P_c^r = v > 0$, and $(\bar{y},\bar{v})$, $\bar{y} > 0, \bar{v} > 0$ be the equilibrium point. Also, assume y^* is chosen such that the allowable maximum value of y is $\tilde{y}^* = \frac{k_c^r}{(k_c^r + G_c^r)} y^*$, i.e. when $y \to \tilde{y}^*$, protective circuits will kick in and limit the dc voltage. Define, $x = y - \bar{y} \Rightarrow y = x + \bar{y}$, $u = v - \bar{v} \Rightarrow v = u + \bar{v}$. Now, (7d) can be written as:

$$\dot{x} = \frac{1}{C_c^r}\left[-G_c^r(x+\bar{y}) + i_{dc}^{max,r}\, sat\left(\frac{k_c^r(y^* - x - \bar{y})}{i_{dc}^{max,r}}\right) - \frac{u+\bar{v}}{x+\bar{y}}\right] \quad (8)$$

This equation is in the form $\dot{x} = f(x,u)$, $x = h(x)$, where $f : D_x \times D_u \to \mathbb{R}$ is locally Lipschitz in (x,u), $h : D_x \to D_x$ is continuous in (x,u), $f(0,0) = 0$, and domains $D_x = (-\bar{y},\ \tilde{y}^* - \bar{y}) \subset \mathbb{R}, D_u \subset \mathbb{R}$ contain the origin. The equilibrium $(\bar{y},\bar{v})$ satisfies the following equation:

$$\bar{v} = \begin{cases} f_1 : -G_c^r\bar{y}^2 + k_c^r\bar{y}(y^* - \bar{y}), & if \quad |k_c^r(y^* - \bar{y})| \le i_{dc}^{max,r} \\ f_2 : -G_c^r\bar{y}^2 + \bar{y} i_{dc}^{max,r}, & otherwise \end{cases}$$

It can be shown that the maximum values of $f_1(.)$ and $f_2(.)$ are obtained at $\bar{y}_{m1} = \frac{k_c^r}{2(G_c^r + k_c^r)} y^*$ and $\bar{y}_{m2} = \frac{i_{dc}^{max,r}}{2G_c^r}$, respectively. Moreover, the point of intersection of $f_1(.)$ and $f_2(.)$ is $y_m = y^* - \frac{i_{dc}^{max,r}}{k_c^r}$.

Depending upon the value of y corresponding to the maxima of $\bar{v}$, we can get four types of characteristics in $y - v$ plane as shown in Fig. 5. For example, type (d) corresponds to $\bar{y}_{m2} \le y_m \le \bar{y}_{m1}$; type (c) occurs for $\bar{y}_{m1} \ge y_m$, $\bar{y}_{m2} > y_m$; type (b) for $\bar{y}_{m1} < y_m$, $\bar{y}_{m2} < y_m$; and type (a) corresponds to $\bar{y}_{m1} < y_m$, $\bar{y}_{m2} > y_m$. Out of these, the typical case is that in Fig. 5(a) – going forward, unless otherwise mentioned, we will consider this characteristic. We note that for any given $\bar{v}$, there exists two equilibria $\bar{y}_1 \in \Omega_1 = [y_m, \tilde{y}^*)$ and $\bar{y}_2 \in \Omega_2 = (0, y_m]$.

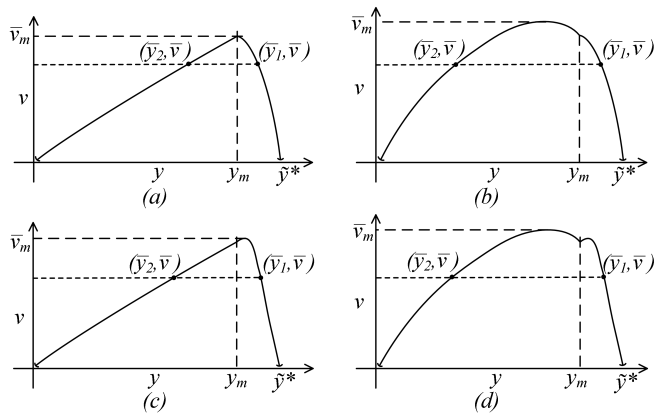

Fig. 5. Four possible v vs y (GFC power vs dc-link voltage) characteristics.

C. Reduced-order Model of Class-B GFCs

Combining (1b) and (5), we can write:

$$C_c^r \dot{v}_{dc}^r = -G_c^r v_{dc}^r + i_{dc}^{max,r} sat\left(\frac{G_c^r v_{dc}^r + \frac{P_c^{r*}}{v_{dc}^{r*}} + k_c^r\left(v_{dc}^{r*} - v_{dc}^r\right)}{i_{dc}^{max,r}}\right) - \frac{P_c^r}{v_{dc}^r} \tag{9}$$

With matching control law $k_m^r v_{dc}^r = \omega_c^r$ and $k_m^r v_{dc}^{r*} = \omega^* = 1pu$, we can modify (9) and (7a)-(7c) to derive the system model with class-B GFCs. In presence of matching control, we assume that $\omega_c^r \approx \omega_{COI} \Rightarrow \underline{\omega}_c^r \approx \underline{\omega}_{COI} = \omega_{COI} - \omega^*$. With this approximation, we can write:

$$\begin{aligned}\frac{C_c^r}{k_m^{r\,2}}\dot{\underline{\omega}}_{COI} &= \underline{P}_c^{max,r} sat\left(\frac{-\frac{k_c^r}{k_m^{r2}}\underline{\omega}_{COI}}{\underline{P}_c^{max,r}}\right) + P_c^{r*} - P_c^r\frac{\omega^*}{\omega_{COI}} \\ &\approx \underline{P}_c^{max,r} sat\left(\frac{-d_{pc}^r\underline{\omega}_{COI}}{\underline{P}_c^{max,r}}\right) - \underline{P}_c^r\end{aligned} \tag{10}$$

With $\frac{C_c^r}{k_m^{r\,2}} \approx 0$ as assumed in [9] and defining $\kappa^r = \frac{d_{pc}^r\underline{\omega}_{COI}}{\underline{P}_c^{max,r}}$, we can write:

$$\underline{P}_c^r = -\underline{P}_c^{max,r} sat\left(\kappa^r\right) \tag{11}$$

where, $d_{pc}^r = \frac{k_c^r}{k_m^{r2}}$, $\underline{P}_c^{max,r} = v_{dc}^{r*} i_{dc}^{max,r} - G_c^r v_{dc}^{r*2} - P_c^{r*}$, $\underline{P}_c^r = P_c^r - P_c^{r*}$. With power balance under nominal condition, i.e. $-P_{gT}^* - P_{cT}^* + P_{LT}^* = 0$, we can write:

$$\begin{aligned}\dot{\underline{\omega}}_{COI} &= \tfrac{1}{2H_T}\left(\underline{P}_{\tau gT} - \sum_{r=1}^{n_1}\underline{P}_c^{max,r} sat\left(\kappa^r\right) - \underline{P}_{LT} - k_{dT}\underline{\omega}_{COI}\right) \\ \dot{\underline{P}}_{\tau gT} &= \tfrac{1}{\tau_{gT}}\left(-\underline{P}_{\tau gT} - d_{pgT}\underline{\omega}_{COI}\right)\end{aligned} \tag{12}$$

where, $\underline{P}_{\tau gT} = P_{\tau gT} - P_{gT}^*$; $\underline{P}_{LT} = P_{LT} - P_{LT}^*$.

D. Model for Stability Analysis of Class-B GFCs

In contrast, to its class-A counterpart, the class-B GFC has a 'feedback mechanism' from the dc-link voltage dynamics to the rest of the system that can alter the power P_c demanded from the GFC. Thus, the stability of dc-link voltage can not be analyzed in isolation and a reduced-order model (12) is used for this purpose. Assuming $z = \left[\underline{\omega}_{COI} \;\; \underline{P}_{\tau gT}\right]^T$, $w = -\underline{P}_{LT}$, (12) can be expressed as $\dot{z} = g(z,w)$, $g : \mathbb{R}^2 \times \mathbb{R} \to \mathbb{R}^2$, where g is locally Lipschitz in (z,w), and $g(0,0) = 0$.

The fundamental difference between these two classes is coming from the fact that class-B GFC controls the frequency based on the dc-link voltage v_{dc}, whereas class-A GFC's frequency regulation is not sympathetic to v_{dc}.

IV. Response Comparison & Limitations: Detailed Model & Reduced Model

First, the reduced-order models as described in (7) and (12) are used to compare the time-domain responses of class-A and class-B GFCs, respectively with those of the detailed models described in Section II-A. Next, the implications of a more detailed dc current source model is investigated. Finally, the limitations of the proposed models are discussed.

A. Response Comparison of Reduced & Detailed Models

1) Class-A GFC: The modified version of the IEEE 68-bus, 16-machine, 5-area system with 4 class-A GFCs (see, Fig. 14) is modeled using both the detailed phasor model as shown in Fig. 2 and the reduced-order model as described in (7). At $t = 0.5$ s a step increase is provided in the load at bus 26 where GFC-2 is also connected. As observed from Fig. 6, the reduced-order model closely approximates the response of the detailed model.

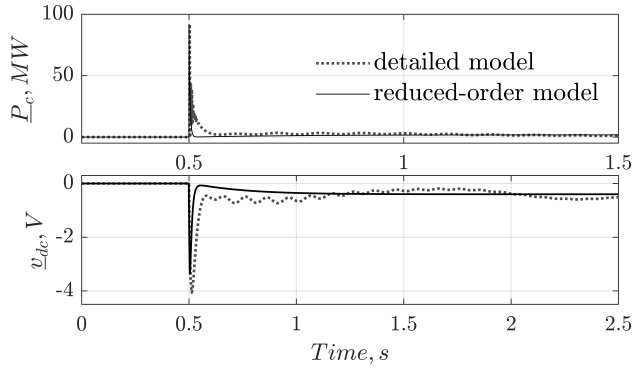

Fig. 6. Comparison of detailed and reduced-order model for GFC-2 in modified IEEE 68-bus, 16-machine, 5-are system with class-A GFCs.

2) Class-B GFC: For class-B GFCs in the modified IEEE 68-bus, 16-machine, 5-area system, the detailed model and the reduced-order model per (12) are compared in a time-domain response. The detailed model considers 6 GFCs as described in section VI-B3. At $t = 0$ s, the $P_{\tau gT}$ state is perturbed to 1.1 times its nominal value, which results in similar responses

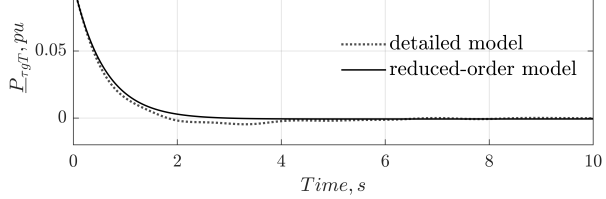

Fig. 7. Comparison of detailed and reduced-order model of the IEEE 68-bus, 16-machine, 5- area system with class-B GFCs.

from both models (see, Fig. 7). The reduced-order model takes into account the equivalent damping torque coefficient k_{dT}.

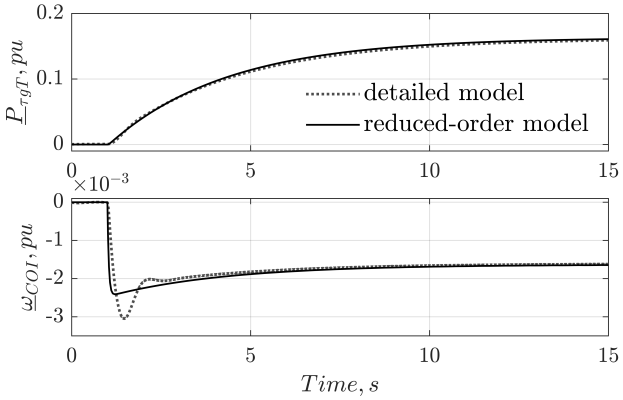

Fig. 8. Comparison of detailed and reduced-order model for modified 9-bus system with class-B GFCs.

As shown in Fig. 8, response from the reduced model show close similarity with a detailed switched model of 9-bus system in Fig. 16(a) following an increase in the total load of the system by 50 MW at $t = 1$ s.

B. Implication of a More Detailed DC Current Source Model

To understand the implications of a more detailed model of the dc current source, a Type-4 wind plant [16] is included at bus 12 of the modified IEEE 4-machine, 2- area system as shown in Fig. 16(b). The SG at bus 1 now serves 50% of its nominal generation (700 MW) and the wind plant serves the rest (350 MW). The grid-side converter (C2) of the wind plant (see, Fig. 9) is operating as a GFC. In two separate cases, the GFC is modeled with class-A and class-B control strategies. The stator-side converter (C1) is operating in grid following mode connected to a synchronous machine as shown in Fig. 9. Converter C1 uses a PLL for the standard vector-control, within which the d-axis current reference is decided based on the $v_{dc} - i_{dc}$ droop as described in (5). The value of i_{dc}^{max} is decided by the MPP of the wind plant's power-speed characteristics at current wind speed. In the phasor simulation model, a functional representation of the wind plant and converter C1 is used as shown in Fig. 9. The power and rotor

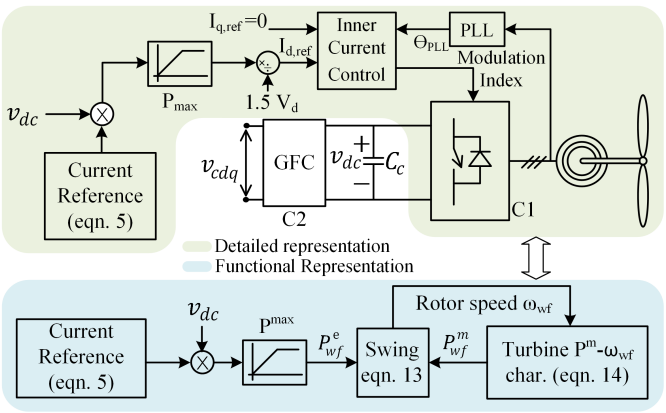

Fig. 9. Detailed and functional model of the wind plant: C1 is stator-side converter and C2 is grid-side converter.

speed dynamics are decided by the swing equation as shown in (13).

$$\dot{\omega}_{wf} = \frac{\omega^*}{2H_{wf}} \left(P^m_{wf} - P^e_{wf}\right) \tag{13}$$

The power-speed characteristics of the wind turbine is described in (14), where the mechanical power depends on the power coefficient of the turbine c_p, which is a function of ω_{wf}, v_{wind}, and β_1.

$$P^m_{wf} = c_p \left(\omega_{wf}, v_{wind}, \beta_1\right) \frac{\rho A}{2} v^3_{wind} \tag{14}$$

Note that the WF is operating in a *deloaded* (i.e. off-MPP) condition.

The issue of dc-link voltage collapse in class-A GFC after a large load increase does not get affected in presence of the the detailed wind plant in the model. In Fig. 10, it is shown that the dc-link voltage of the class-A GFC in the 4-machine system collapses when the total load increases by 40%, but it is stable for a smaller load increase (e.g., 20%). This time-domain response also shows the fast dc-voltage dynamics and much slower rotor dynamics of the wind plant. For the stable case, the turbine rotor speed settles at a lower value in order to produce higher power output.

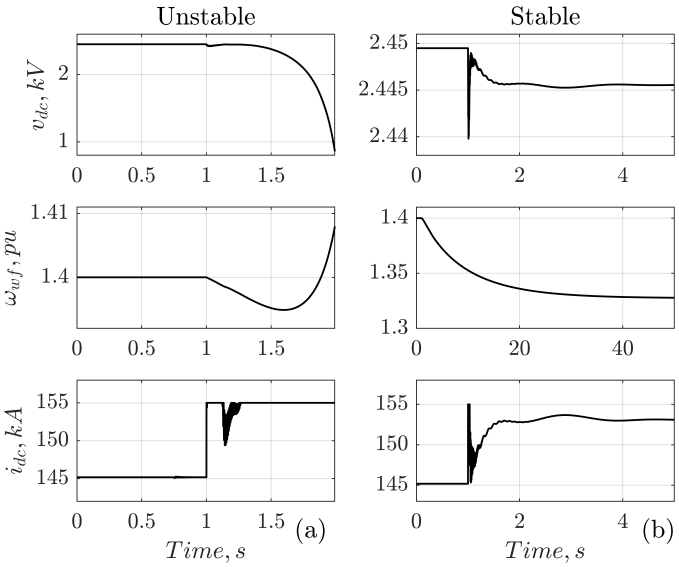

Fig. 10. Wind plant with class A GFC in IEEE 4-machine system: (a) unstable dc link voltage after 40% increase in all the loads, (b) stable dc link voltage after 20% increase in all the loads.

As shown in [8], [9], the dc-link voltage of the class-B GFC is less likely to collapse during a large load increase. In Fig. 11 (b), it is shown that a 40% increase in the total load of the modified 4-machine system does not cause any instability in the dc-link voltage of the class-B GFC. However, if i_{dc}^{max} is chosen to be higher than the maximum power limitation from the wind plant, the converter might try to deliver more power than the MPP of the speed-power characteristics of the wind plant after a large load increase. It might slow down the rotor of the wind plant and eventually, it will stall as shown in Fig. 11(a).

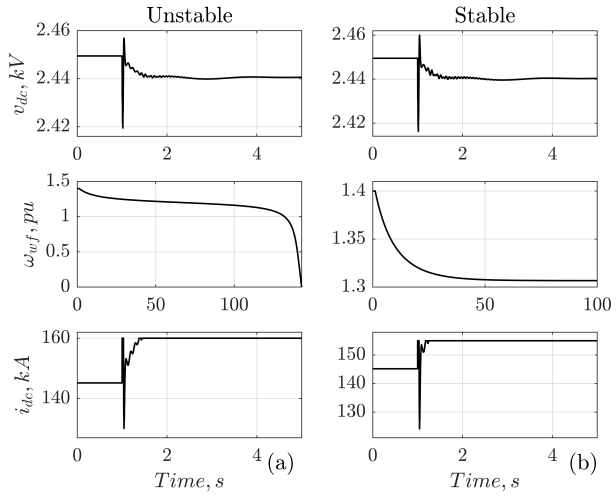

Fig. 11. Wind plant with class B GFC in IEEE 4-machine system: (a) rotor stalls when i_{dc}^{max} is higher than MPP at current wind speed, (b) stable when i_{dc}^{max} is decided considering the power limitation from plant.

C. Discussion on Limitations of the Proposed Models

First, we remark on the limitation of the proposed detailed models. After that, we focus on the limitations of the reduced models.

1) The detailed model with dc-side current representation is adequate for studying dc-link voltage instability as long as i_{dc}^{max} corresponds to the MPP of the dc-side source.
2) Components like damper windings and power system stabilizers (PSSs), among others are not included in the reduced-order models, which makes the stability analysis in presence of class-B GFCs more *conservative*. One way to capture the net damping effect is to use total damping torque coefficient k_{dT} as in (7)(b), which needs to be determined by comparing the COI frequency dynamics with a detailed model through trial-and-error method.
3) The reduced-order model considers constant power load. However, this model cannot capture voltage or angle stability issues induced by such loads in the detailed model. Moreover, for a heavily-stressed power system, voltage, angle, and frequency instabilities can get coupled, which cannot be captured by the reduced model.

V. Stability Analysis Under DC-side Current Limits During Primary Frequency Response

We focus on stability analysis of v_{dc} in presence of dc-side current limits when the GFCs participate in primary frequency response. To that end, we establish the following: (1) Lyapunov stability and region of attraction (ROA)[1] for class-A and class-B GFCs, (2) Sufficiency condition for input-output stability of class-A GFCs, (3) Sufficiency condition for instability of class-A GFCs, and (4) Sufficiency condition for input-to-state stability[2] for class-B GFCs.

A. Stability Analysis of Class-A GFC

We first focus on the reduced model of the test system in Fig. 4 and present the following Theorems and Lemmas.

Theorem V.1. *For class-A GFCs, the equilibrium $\bar{y}_1$ is asymptotically stable with ROA $\mathcal{R}_{\mathcal{A}} = (\bar{y}_2, \tilde{y}^*)$.*

Proof. Corresponding to the domain Ω_1 for y, (8) can be rewritten as:

$$\dot{x} = \frac{1}{C_c^r}\left[-G_c^r x - k_c^r x + \frac{\bar{v}}{\bar{y}_1}\frac{x}{x+\bar{y}_1} - \frac{u}{x+\bar{y}_1}\right] \tag{15}$$

where, $x \in \tilde{D}_x = [y_m - \bar{y}_1,\ \tilde{y}^* - \bar{y}_1) \subset D_x,\ u \in D_u$. Consider the following Lyapunov function

$$V_1 = \frac{C_c^r}{2}x^2,\ x \in \tilde{D}_x$$

Now, we can write the unforced system as:

$$\dot{V}_1 = \left[-(G_c^r + k_c^r) + \frac{\bar{v}}{\bar{y}_1}\frac{1}{x+\bar{y}_1}\right]x^2$$

It can be shown that $\dot{V}_1$ is negative definite, if $x > \tilde{y}^* - 2\bar{y}_1$. In the most typical case as in Fig. 5(a), $\bar{y}_1 > y_m > (\tilde{y}^*/2)$, which satisfies this condition. Therefore, $\bar{y}_1$ is asymptotically stable $\forall y \in \Omega_1$.

To establish the ROA of $\bar{y}_1$, we analyze Lyapunov stability of $\bar{y}_2 \in \Omega_2$ shown in Fig. 5(a) with the same $\bar{v}$. To that end, we can rewrite (8) with $u = 0$ as:

$$\dot{x} = \frac{1}{C_c^r}\left[-G_c^r(x+\bar{y}_2) + i_{dc}^{max,r} - \frac{\bar{v}}{x+\bar{y}_2}\right], x \in \bar{D}_x = (-\bar{y}_2, y_m - \bar{y}_2]$$

Choosing a continuously differentiable function

$$V_2 = \frac{C_c^r}{2}\left[\bar{y}_2^2 - (x+\bar{y}_2)^2\right],\quad x \in \bar{D}_x,\quad \text{s.t. } V_2(0) = 0$$

We choose a ball $B_r = \{x\ \in \mathbb{R}\ \mid\ |x| \le r\}$ and define set $U = \{x\ \in B_r\ \mid\ V_2 > 0\}$ – note that $U \subseteq (-\bar{y}_2, 0)$. Therefore, we can choose $x(0) = x_0 \in U$ arbitrarily close to the origin s.t. $V_2(x_0) > 0$. Also,

$$\dot{V}_2 > 0,\ \forall x\ \in U,\quad \text{if } x < \frac{i_{dc}^{max,r}}{G_c^r} - 2\bar{y}_2$$

Taking into account the typical characteristics in Fig. 5(a) and analyzing local maxima of f_2, we can write $\bar{y}_2 < (i_{dc}^{max,r}/2G_c^r)$. Therefore, $\dot{V}_2 > 0, \forall x\ \in U$, which provides a sufficiency condition for instability of $\bar{y}_2$ following Chetaev's theorem [17]. This implies that $y(t)$ with any initial value $y(0) = y_0 \in (0, \bar{y}_2) \subset \Omega_2$ will move away from $\bar{y}_2$ and reach 0.

Next, consider a continuously differentiable function

$$V_3 = \frac{C_c^r}{2}\left[(x+\bar{y}_2)^2 - \bar{y}_2^2\right],\quad x \in \bar{D}_x,\quad \text{s.t. } V_3(0) = 0$$

[1][17] Let $\phi(t;z)$ (defined $\forall t \ge 0$) be the solution of $\dot{z} = f(z)$ that starts at initial value z at $t = 0$, then the ROA of an asymptotically stable equilibrium $z = 0$ of this system is defined as $\left\{z \middle| \lim_{t\to\infty}\phi(t;z) = 0\right\}$.

[2][17] The system $\dot{z} = f(t,z,u)$, $f : [0,\infty) \times \mathbb{R}^n \times \mathbb{R}^m \to \mathbb{R}^n$ piecewise continuous in t and localy Lipschitz in z and u, is input-to-state stable if there exist a class $\mathcal{KL}$ function β and a class $\mathcal{K}$ function γ such that for any initial state $z(t_0)$ and any bounded input $u(t)$, the solution $x(t)$ exists for all $t \ge t_0$ and satisfies $||z(t)|| \le \beta(||z(t_0)||, t - t_0) + \gamma\left(\sup_{t_0 \le \tau \le t}||u(\tau)||\right)$.

It is easy to follow similar arguments and show that

$$V_3 > 0, \forall x \in (0, y_m - \bar{y}_2] \subset \tilde{D}_x$$

This implies that $y(t)$ with any initial value $y_0 \in \bar{\Omega}_2 = (\bar{y}_2, y_m] \subset \Omega_2$ will move away from $\bar{y}_2$ and reach y_m. We define $\mathcal{R}_{\mathcal{A}} = \bar{\Omega}_2 \bigcup \Omega_1 = (\bar{y}_2, \tilde{y}^*)$, which is the largest open, connected, invariant set in $\Omega_2 \bigcup \Omega_1$, such that $\lim_{t\to\infty} y(t) = \bar{y}_1, \forall y(0) \in \mathcal{R}_{\mathcal{A}}$. This implies $\mathcal{R}_{\mathcal{A}}$ is the ROA for equilibrium $\bar{y}_1$ of class-A GFCs. □

Corollary V.1.1. *For class-A GFCs, the equilibrium $\bar{y}_1$ is exponentially stable in Ω_1.*

Proof. As mentioned in Theorem V.1, the chosen Lyapunov function is

$$V_1 = \frac{C_c^r}{2} x^2 = \frac{C_c^r}{2} |x|^2, \quad x \in \tilde{D}_x$$

Also,

$$\dot{V}_1 \leq \left[-(G_c^r + k_c^r) + \frac{\bar{v}}{\bar{y}_1} \frac{1}{y_m} \right] |x|^2, \; x \in \tilde{D}_x$$

Since, $m = -(G_c^r + k_c^r) + \frac{\bar{v}}{\bar{y}_1} \frac{1}{y_m} < 0$, it satisfies all conditions in Theorem 4.10 in [17], and therefore $\bar{y}_1$ is exponentially stable in Ω_1. □

Theorem V.2. *The dc voltage dynamics of class-A GFCs described in* (8) *is small-signal finite-gain $\mathcal{L}_p$ stable $\forall p \in [1, \infty]$, if $x(0) = x_0 \in \{|x| \leq r\} \subset \tilde{D}_x$, $r > 0$. Also, for a $r_u > 0$, s.t. $\{|u| \leq r_u\} \subset D_u$, $r_u > 0, \forall u \in \mathcal{L}_{pe}$ with $\sup_{0 \leq t \leq \tau} |u| \leq \min\{r_u, |m| y_m r\}$, the output $x(t)$ is bounded by the following relation $\|x_\tau\|_{\mathcal{L}_p} \leq \frac{\|u_\tau\|_{\mathcal{L}_p}}{|m| y_m} + \beta \quad \forall \tau \in [0, \infty)$, where $\beta = |x_0|$, if $p = \infty$, and $\left(\frac{C_c^r}{p|m|} \right)^{\frac{1}{p}} |x_0|$, if $p \in [1, \infty)$.*

Proof. We proved that $x = 0$ is exponentially stable in $\tilde{D}_x$ in Corollary V.1.1. With Lyapunov function

$$V_1 = \frac{C_c^r}{2} x^2 = \frac{C_c^r}{2} |x|^2$$

we have $\dot{V}_1 \leq -|m||x|^2$, $\left| \frac{\partial V_1}{\partial x} \right| = C_c^r |x|$, $\forall x \in \tilde{D}_x$. Also, $|f(x,u) - f(x,0)| \leq \frac{1}{C_c^r y_m} |u|, |h(x,u)| = |x|, \; \forall x \in \tilde{D}_x, \; \forall u \in D_u$. This satisfies all conditions in Theorem 5.1 in [17] and proves the conditions for input-output stability and bound on output. □

Remark I: It can be shown that $\min\{r_u, |m| y_m r\} = \underline{P}_c^{max}$ in Theorem V.2. Moreover, the dc-link voltage trajectory should satisfy the following constraint $y_m \leq v_{dc}(t) < \tilde{y}^*, \; t \in [0, \infty)$, which restricts the initial state $v_{dc}(0)$ to the same range.

Theorem V.3. *For class-A GFCs, the equilibrium $\bar{y}_1 \in \Omega_1$ of* (8) *with $u = 0$ is unstable if*

$$\bar{v} > -G_c^r (x + \bar{y}_1)^2 + (x + \bar{y}_1) i_{dc}^{max,r} sat\left(\frac{k_c^r (y^* - x - \bar{y}_1)}{i_{dc}^{max,r}} \right)$$

for any $x \in [-r, \; 0)$, where $r = \min\{\bar{y}_1, \tilde{y}^* - \bar{y}_1\}$.

Proof. The unforced system can be expressed as

$$\dot{x} = \frac{1}{C_c^r} \left[-G_c^r (x + \bar{y}_1) + i_{dc}^{max,r} sat\left(\frac{k_c^r (y^* - x - \bar{y}_1)}{i_{dc}^{max,r}} \right) - \frac{\bar{v}}{x + \bar{y}_1} \right]$$

$\forall x \in D_x \subset \mathbb{R}$. Define a continuously differentiable function,

$$V_4 : D_x \to \mathbb{R}, \quad V_4(x) = \frac{1}{2} C_c^r \left[\bar{y}_1^2 - (x + \bar{y}_1)^2 \right], \quad \text{s.t. } V_4(0) = 0$$

Choose $r \in (0, \min\{\bar{y}_1, \tilde{y}^* - \bar{y}_1\}]$ such that the ball $B_r = \{x \in \mathbb{R} | \; |x| \leq r\}$, $B_r \subset D_x$. Define, $U = \{x \in B_r | V_4(x) > 0\}$, implying $U = [-r, \; 0)$. Choose x_0 in the interior of $U \implies x_0 < 0$. Hence, $V_4(x_0) > 0$ for any such x_0 arbitrarily close to the origin. Now, derivative of V_4 along the trajectory of x is:

$$\dot{V}_4 = G_c^r (x + \bar{y}_1)^2 - (x + \bar{y}_1) i_{dc}^{max,r} sat\left(\frac{k_c^r (y^* - x - \bar{y}_1)}{i_{dc}^{max,r}} \right) + \bar{v}$$

According to Chetaev's theorem [17], the sufficiency condition for instability is $\dot{V}_4 > 0, \; \forall x \in U$, which proves the theorem.

□

B. Stability Analysis of Class-B GFC

In this section, we analyze the stability of class-B GFCs and present the following lemma and theorem.

Lemma V.4. *For class-B GFCs, the equilibrium $z = 0$ is globally asymptotically stable $\forall \, d_{pgT}, \; d_{pc}^r > 0, \; \forall r$.*

Proof. For unforced system, $w = -\underline{P}_{LT} = 0$. Choose Lyapunov function with $d_{pgT} > 0$, $V_5 = H_T \underline{\omega}_{COI}^2 + \frac{\tau_{gT}}{2 d_{pgT}} \underline{P}_{\tau gT}^2$.

$$\Rightarrow \dot{V}_5 = -\frac{\underline{P}_{\tau gT}^2}{d_{pgT}} - \underline{\omega}_{COI} \sum_{r=1}^{n_1} \underline{P}_c^{max,r} sat(\kappa^r) - k_{dT} \underline{\omega}_{COI}^2 \quad (16)$$

Here, $\underline{\omega}_{COI} \sum_{r=1}^{n_1} \underline{P}_c^{max,r} sat(\kappa^r) > 0 \quad \forall \, \underline{\omega}_{COI} \in \mathbb{R} - \{0\}, \; d_{pc}^r > 0$. Thus, $\dot{V}_5$ is negative definite and radially unbounded $\forall \, d_{pgT}, \; d_{pc}^r, \; k_{dT} > 0$. Therefore, the origin is globally asymptotically stable when this condition is satisfied. □

Remark II: We observe that the ROA for $x = 0$ corresponding to the equilibrium $\bar{y}_1$ of class-A GFCs is limited to $x \in (\bar{y}_2 - \bar{y}_1, \tilde{y}^* - \bar{y}_1)$, while the same for $z = 0$ of class-B GFCs is $\mathbb{R}^2$. Also, equilibrium $\bar{y}_2$ of class-A GFCs is unstable.

For studying input-to-state stability, we will assume $k_{dT} = 0$, which will lead to a conservative analysis.

Theorem V.5. *The reduced-order model* (12) *is input-to-state stable with class $\mathcal{KL}$ function β and class $\mathcal{K}$ function $\gamma(|w|) = c \max\{\chi_1(|w|), \chi_2(|w|)\}, \; c > 0$ for piecewise continuous $w(t)$ that is bounded in t, $\forall t \geq 0$ implying $\|z(t)\| \leq \beta(\|z(t_0)\|, t - t_0) + \gamma\left(\sup_{\tau \geq t_0} |w(\tau)| \right), \forall t \geq t_0$, where, $(\underline{P}_c^{\max}, \; d_{pc}) = \underset{\underline{P}_c^{\max,r}, d_{pc}^r}{\arg\min} \underline{P}_c^{\max,r} \tanh(|\kappa^r|), r = 1 : n_1; \chi_1(|w|) = \frac{\underline{P}_c^{\max}}{d_{pc}} \tanh^{-1}\left(\frac{|w|}{\theta n_1 \underline{P}_c^{\max}} \right)$, and $\chi_2(|w|) = \left[\frac{|w| d_{pgT}}{\theta} \chi_1(|w|) \right]^{\frac{1}{2}}$ $\forall w \in (-\theta n_1 \underline{P}_c^{\max}, \; \theta n_1 \underline{P}_c^{\max})$, $\underline{P}_c^{\max} \in \mathbb{R}_{>0}$, $0 < \theta < 1$, $\mathbb{R}_{>0}$: positive real space.*

Proof. In Lemma V.4, it is shown that $\dot{z} = g(z,0)$ is globally asymptotically stable. It can be shown that the Lyapunov function $V_5(z)$ satisfies the following inequalities:

$$\lambda_{\min}(Q)\|z\|_\infty^2 \le V_5(z) \le (\lambda_{\max}(Q)+\lambda_{\min}(Q))\|z\|_\infty^2$$
$$\Rightarrow \alpha_1(\|z\|) \le V_5(z) \le \alpha_2(\|z\|)$$

where α_1 and α_2 are class $\mathcal{K}_\infty$ functions and $Q = \begin{bmatrix} H_T & 0 \\ 0 & \frac{\tau_{gT}}{2d_{pgT}} \end{bmatrix}$. For $0<\theta<1$, we can write:

$$\dot{V}_5 = -\frac{\underline{P}^2_{\tau gT}}{d_{pgT}} - \underline{\omega}_{COI}\sum_{r=1}^{n_1}\underline{P}_c^{\max,r} sat(\kappa^r) + w\underline{\omega}_{COI}$$
$$\le -(1-\theta)\left(\frac{\underline{P}^2_{\tau gT}}{d_{pgT}} + \underline{\omega}_{COI}\sum_{r=1}^{n_1} P_c^{\max,r} sat(\kappa^r)\right)$$
$$-\theta\left(\frac{\underline{P}^2_{\tau gT}}{d_{pgT}} + \underline{\omega}_{COI}\sum_{r=1}^{n_1} P_c^{\max,r} sat(\kappa^r)\right) + |w|\,|\underline{\omega}_{COI}|$$

Let us define, $W = (1-\theta)\left(\frac{\underline{P}^2_{\tau gT}}{d_{pgT}} + \underline{\omega}_{COI}\sum_{r=1}^{n_1} P_c^{\max,r} sat(\kappa^r)\right)$, which is a positive definite function in $\mathbb{R}^2$. Now, define

$$\Gamma = -\theta\left(\frac{\underline{P}^2_{\tau gT}}{d_{pgT}} + \underline{\omega}_{COI}\sum_{r=1}^{n_1} P_c^{\max,r} sat(\kappa^r)\right) + |w|\,|\underline{\omega}_{COI}|$$

As, tanh is a class $\mathcal{K}$ function and $\tanh(\kappa^r) < sat(\kappa^r)$, replacing saturation with tanh function and assuming $\underline{P}_c^{\max}\tanh\left(\left|\frac{d_{pc}}{\underline{P}_c^{\max}}\underline{\omega}_{COI}\right|\right) = \min\left(\underline{P}_c^{\max,r}\tanh(|\kappa^r|)\right) =$ $\min\left(\underline{P}_c^{\max,r}\tanh\left(\left|\frac{d^r_{pc}}{\underline{P}_c^{\max,r}}\underline{\omega}_{COI}\right|\right)\right)$, $r = 1:n_1$, we can write

$$\Gamma < -\theta\left(\frac{\underline{P}^2_{\tau gT}}{d_{pgT}} + \underline{\omega}_{COI} n_1 \underline{P}_c^{\max}\tanh\left(\left|\frac{d_{pc}}{\underline{P}_c^{\max}}\underline{\omega}_{COI}\right|\right)\right) + |w|\,|\underline{\omega}_{COI}|$$

Now, this term Γ will be ≤ 0 if $|\underline{\omega}_{COI}| \ge \frac{\underline{P}_c^{\max}}{d_{pc}}\tanh^{-1}\left(\frac{|w|}{\theta n_1 \underline{P}_c^{\max}}\right) = \chi_1(|w|)$ or $|\underline{\omega}_{COI}| \le \chi_1(|w|)$ and $\left|\underline{P}_{\tau gT}\right| \ge \left[\frac{|w| d_{pgT}}{\theta}\chi_1(|w|)\right]^{\frac{1}{2}} = \chi_2(|w|)$. This condition implies $\|z\|_\infty \ge \max\{\chi_1(|w|), \chi_2(|w|)\} = \rho(|w|)$. So,

$$\dot{V}_5 \le -W, \quad \forall \|z\|_\infty \ge \rho(|w|)$$

Here, $\rho(|w|)$ is a class $\mathcal{K}$ function with $w \in (-\theta n_1 \underline{P}_c^{\max},\ \theta n_1 \underline{P}_c^{\max})$. Since, $\underline{P}_c^{\max} \in \mathbb{R}_{>0}$, we contend that the above holds $\forall (z,w) \in \mathbb{R}^2 \times \mathbb{R}$. Therefore, we have satisfied all conditions of input-to-state stability per Theorem 4.19 in [17]. Now, we need to define class $\mathcal{K}$ function $\gamma = \alpha_1^{-1} \circ \alpha_2 \circ \rho$. It can be shown that $\gamma(|w|) = \sqrt{\frac{\lambda_{\max}(Q)+\lambda_{\min}(Q)}{\lambda_{\min}(Q)}}\rho(|w|) = c\rho(|w|)$. □

Remark III: Unlike class-A GFC, the initial states $z(t_0) \in \mathbb{R}^2$. However, in reality, the assumptions behind the reduced-order model (12) will hold for a subset of initial states when a detailed model is considered. This will be demonstrated through case studies in the next section.

C. Engineering Applications of the Proposed Analysis

The proposed Theorems, Lemmas, and Corollaries give certain sufficiency conditions for stability and bounds on variations of dc-link voltage following disturbances. Overall, they also give insights into the performance of the two classes of GFCs. An engineer can apply these in the following ways –

- *Bound on dc-link voltage variation of class-A GFCs:* Using Theorem V.2, the limit on dc-link voltage variation following a bounded disturbance in system load/generation can be calculated. The dip in the dc-link voltage is of interest for converter control. *This will not require a complex time-domain simulation.*
- *Maximum allowable load/generation change to guarantee stability of the dc-link voltage:* From Theorem V.5, the maximum load/generation change to guarantee stability of dc-link voltage of class-B GFCs is $n_1\underline{P}_c^{max}$, which can be calculated for any operating point. This will allow operators to compare the loss of power due to $(N-1)$ generator outage contingency and ascertain such guarantees in near real-time. Similar conclusions can be drawn about class-A GFCs from Remark I.
- *Engineering and scientific insights:* The results lead to important insights and stability guarantees that give practicing engineers some guidance on which GFC type may be acceptable given their implementation complexity vs risk of instability trade-off. For example, class-A GFCs can be easier to implement, but would face instability issues if a system's largest generation outage contingency is larger than $n_1\underline{P}_c^{max}$.

VI. Results & Discussions

For verifying the accuracy of the proposed lemmas and theorems, we consider: (a) the detailed switched model of a standalone GFC connected to a constant power load; (b) the detailed switched model of two GFCs connected to the modified 9-bus system available online [18]; and (c), (d) the positive sequence fundamental frequency phasor models of a modified version of the IEEE 4-machine, 2-area system [15] and IEEE 68-bus, 16-machine, 5-area system [19], both with constant power loads. All these simulation models have the detailed controls of the GFC as shown in Fig. 3. These phasor models take into account a sixth-order subtransient model of SGs with excitation systems and the averaged model of GFCs with the control loops described in Section II. The integration of GFCs and SGs with the remaining network in the phasor model is illustrated in Fig. 2. The simulation cases and the verified theorems are summarized in Table I, which are described in detail in the following sections. Parameter k_{dT} is assumed to be zero in the following simulation studies.

A. Class-A GFC

1) Standalone GFC Connected to Load: This system considers all the details of control loops mentioned in section II-B

TABLE I
SIMULATION MODELS FOR VERIFYING THE PROPOSED THEOREMS AND LEMMAS

GFC class	Test case	Simulation platform	Proposition validated
Class - A	Standalone GFC connected to load	Detailed switched model in EMTDC/PSCAD	Theorems V.1 and V.3
	Modified IEEE 4-machine 2-area System	Detailed phasor model in Matlab/Simulink	Theorem V.2
	Modified IEEE 16-machine System		
Class - B	Modified 9-bus System	Detailed switched model in Matlab/Simulink	Lemma V.4 & Theorem V.5
	Modified IEEE 4-machine 2-area System	Detailed phasor model in Matlab/Simulink	Lemma V.4
	Modified IEEE 16-machine System		Lemma V.4 & Theorem V.5

for class-A GFC, which is built using EMTDC/PSCAD [20]. First, we switch the dc bus capacitor voltage to a value y_0 at $t = 0.2$ s while operating at equilibrium $(\bar{y}_1, \bar{v})$. As shown in Fig. 12, the dc-link voltage collapses when $y_0 < \bar{y}_2$, and stable if $y_0 > \bar{y}_2$ by a slight margin. Here, $\bar{y}_1 = 2.4$ kV, and $\bar{y}_2 = 2$ kV corresponding to $\bar{v} = 150$ kW is considered. The results are in agreement with Theorem V.1.

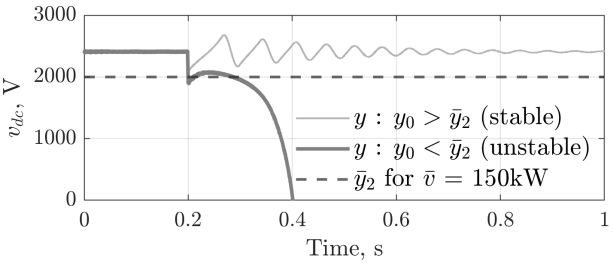

Fig. 12. Standalone Class-A GFC model: unforced response.

Next, we show that v_{dc} is stable following a small step increase in load from $\bar{v} = 175$ kW to $\bar{v}_m = 177$ kW (see, Figs 13(a), (b)), which is in agreement with Theorem V.2. In Fig. 13 (c,d), it is shown that when $v = \bar{v}_m$, the unforced response becomes unstable when the initial value of y is less than y_m, which matches the condition of Theorem V.3.

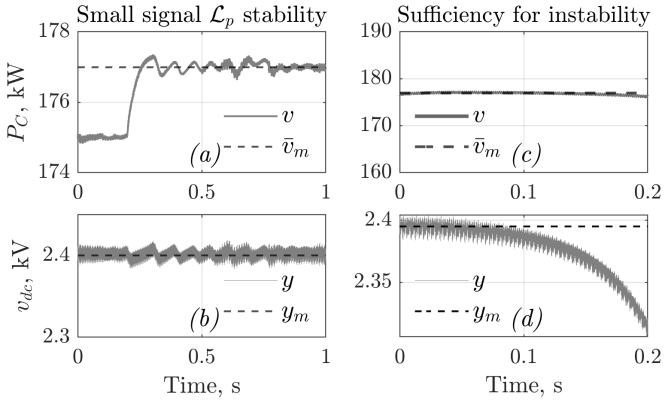

Fig. 13. Standalone Class-A GFC model: (a), (b): Forced response; (c), (d): Unforced response.

2) Phasor Model of Modified IEEE 16*-machine System:* As shown in Fig. 14, we consider the modified phasor model of the IEEE 16-machine system with averaged models of 4 GFCs integrated to it as described in Section II. Among these, 2 are in NETS and 2 are in NYPS, which serve 33% and 23% of the total power generation in the respective areas.

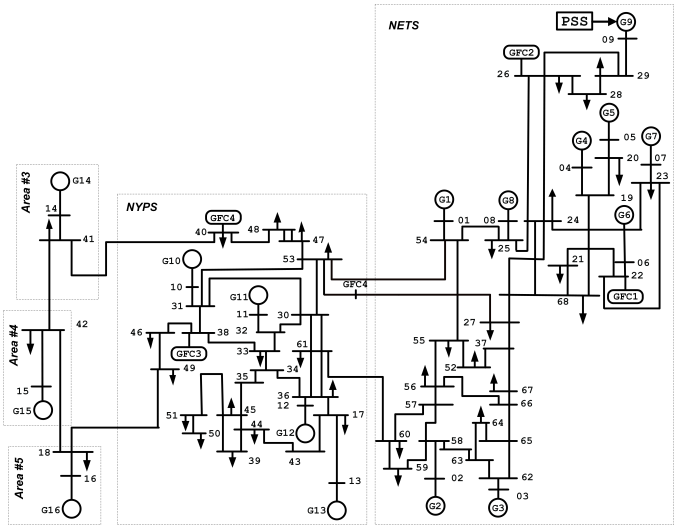

Fig. 14. Single-line diagram of modified IEEE 16-machine system with 4 class-A GFCs. Load type: constant power.

Although we conducted numerous experiments to verify all the Theorems on class-A GFCs in this system, due to space restrictions we only present a case study to check the sufficiency condition of input-to-state stability and bound on $\mathcal{L}_\infty$ norm of the deviation in v_{dc} per Theorem V.2. Figure 15 shows the variation in P_c and v_{dc} of GFC 2 following a step increase in load at bus 26. We note that $\underline{P}_c^{max} = 98$ MW, and therefore $\|u_\tau\|_{\mathcal{L}_p} = 92$ MW satisfies the requirement $\sup_{0<t<\tau} |u| \leq \underline{P}_c^{max}$ per

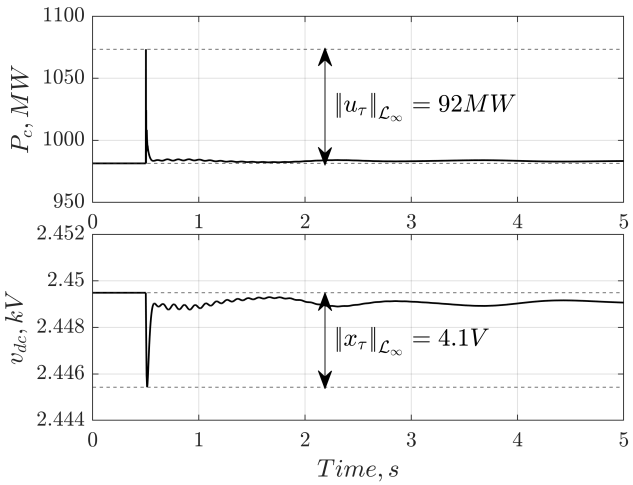

Fig. 15. Power and dc-link voltage variation of GFC 2 in modified IEEE 16-machine system in Fig. 14 following a step increase in load at bus 26.

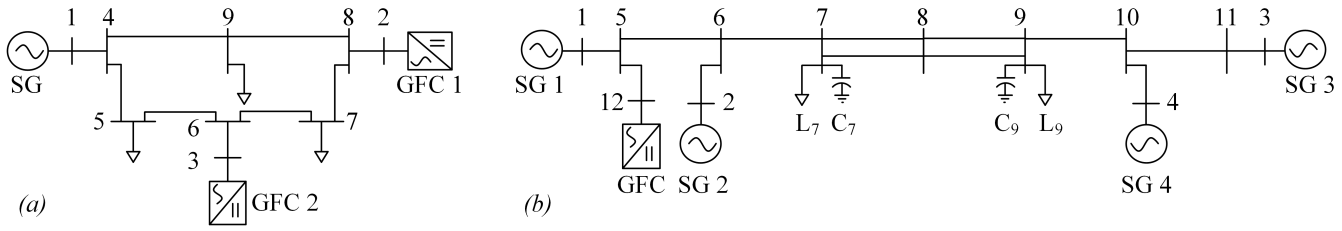

Fig. 16. Line diagram of (a) modified 9-bus test system with 2 GFCs, (b) modified IEEE 4-machine 2-area system. Load type: constant power.

Remark I. We see that v_{dc} is stable following the disturbance as postulated in Theorem V.2. Moreover, for this case the values $|m| = 1.84e3$ Ʊ, $y_m = 2.43$ kV, and $|x_0| = 0$ V lead to a bound of 20.6 V on peak deviation of v_{dc}. As Fig. 15 shows, the actual value of peak deviation is 4.1 V, which respects this bound and satisfies the condition $\{|x| \leq r\} \subset \tilde{D}_x$.

B. Class-B GFC

As described earlier, unlike class-A GFCs, the stability of its class-B counterpart needs to take into account the whole system. Through exhaustive testing in different multimachine systems, we establish the validity and limitations of Lemma V.4 and Theorem V.5.

1) Detailed 3-phase Model of Modified 9-bus System: This test system shown in Fig. 16(a), built in Matlab/Simscape [21], was taken from online resource [18]. However, we changed the loads to constant power type from constant impedance type for validation.

First, we focus on Lemma V.4, which is based on a reduced-order model with simplifying assumptions described in Section III-C. We performed tests with the state variables v_{dc}, $P_{\tau g}$ and ω_g starting from different extremities by resetting their values at a particular instant and observing the unforced response. Figure 17 shows the unforced response of the system when the initial values of the perturbed states are: $v_{dc0} = v^1_{dc}(0.5) = v^2_{dc}(0.5) = 1.2\bar{v}_{dc},\ P_{\tau g0} = P_{\tau g}(0.5) = 3.2\bar{P}_{\tau g}$. Superbars are used to denote pre-disturbance values. The derivative of the Lyapunov function V_5 for unforced system as derived in (16) is also shown here. $\dot{V}_5$ is always negative (except at the origin) which satisfies the asymptotic stability condition according to the Lemma. Although, similar conclusions were obtained from multiple other combinations of initial states. only these cases are reported due to space restriction.

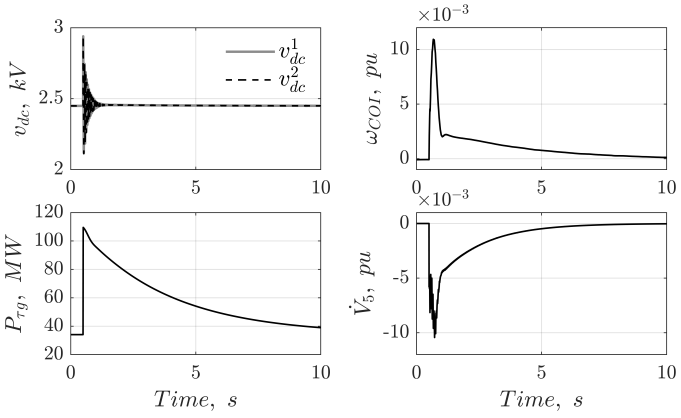

Fig. 17. Unforced response with class-B GFCs in 9-bus system. At $t = 0.5$ s, v_{dc} of GFCs and $P_{\tau g}$ are set to 1.2 and 3.2 times of the steady state values, respectively.

It can be observed that class-B GFCs converge to pre-disturbance equilibria even after starting from such a large off-nominal values. Although, this does not prove the global asymptotic stability as claimed in Lemma V.4, we do find evidence of a significantly large ROA in our tests.

To demonstrate the input-to-state stability of class-B GFCs in 9-bus system per Theorem V.5, a step increase of 10 MW is given in load at bus 7 and the state $P_{\tau g}$ is perturbed to 3.2 times of nominal value at $t = 1$ s. Note that for this system $\theta n_1 \underline{P}^{max}_c = 160$ MW, which is the maximum allowable total load change postulated in the theorem ($0 < \theta < 1, n_1 = 2$, $\underline{P}^{max}_c = 80$ MW). As shown in Fig. 18, the system is stable after this load increase. The constraints on $|\underline{P}_{\tau gT}|$ and $|\underline{\omega}_{COI}|$ that are sufficiency conditions for $\dot{V}_5$ to be negative are satisfied till $t = t_1$ after which $\dot{V}_5$ is almost 0. Following the disturbance, $|\underline{\omega}_{COI}| \geq \chi_1$ till $t = t_2$, whereas $|\underline{\omega}_{COI}| \leq \chi_1$ and $|\underline{P}_{\tau gT}| \geq \chi_2$ during $t_2 \leq t \leq t_1$. We observe that when $\dot{V}_5$ is negative, but very close to zero, the sufficiency conditions are not met, which shows some degree of conservatism in the constraints.

We note that the major issue in simulating such a detailed 3-phase model comes from very high computational burden, which rules out exhaustive case studies. To resolve this, we validate our propositions on class-B GFCs in two positive

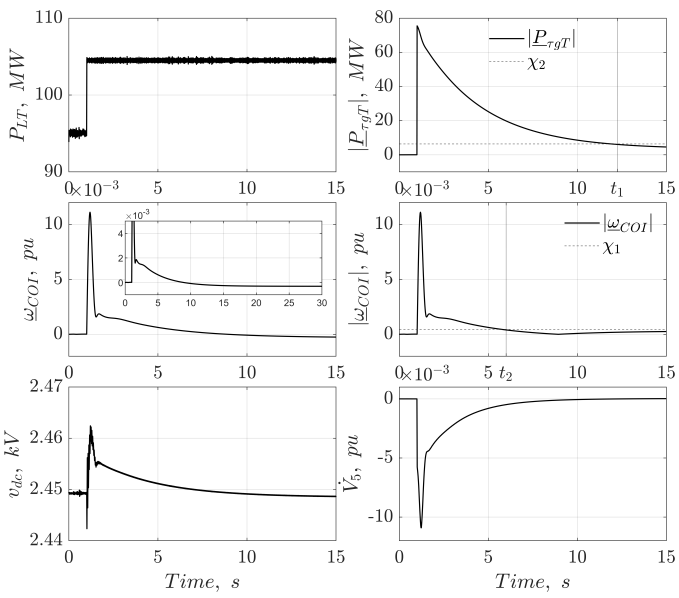

Fig. 18. Forced response of class-B GFCs in 9-bus system following a step increase of 10 MW load at bus 7 at $t = 1$ s, while at the same instant, the initial value of $P_{\tau g0}$ is set to 3.2 times the nominal value.

sequence fundamental frequency test system models integrated with averaged models of GFCs as described in Section II.

2) Phasor Model of Modified IEEE 4-machine 2-area System: In the modified 4-machine system shown in Fig. 16(b), generation from SG1 is decreased to 50% of nominal value (700 MW) and the power deficit (i.e. 350 MW) is produced by the GFC at bus 5. To determine the ROA, we perform a design of experiment on the phase space involving the initial values of state variables $v_{dc}(0)$, $f_{COI}(0)$, and $\underline{P}_{\tau gT}(0)$, where $f_{COI}(0) = \omega_g(0)/(2\pi)$, $\omega_g(0) = \omega_g^r(0)$, $\forall r = 1,\ldots,4$; $\underline{P}_{\tau gT}(0) = \sum_{r=1}^{4} \underline{P}_{\tau g}^r(0)$. To that end, we obtain the unforced response of the system by varying the initial values of these states from their equilibrium $(\bar{v}_{dc},\ \bar{f}_{COI},\ \underline{P}_{\tau gT}) = (2.45\ kV,\ 60\ Hz,\ 0\ MW)$ such that $v_{dc}(0) \in [0.25,\ 2.63]\ kV$, $f_{COI}(0) \in [6,\ 120]\ Hz$, and $\underline{P}_{\tau gT}(0) \in [-24.8e2,\ 74.3e2]\ MW$.

Figure 19 shows the ROA in $v_{dc} - f_{COI} - \underline{P}_{\tau gT}$ space. The region is shown from three different angles in Figs 19(a)-(c) to get a more clear visualization. On the other hand, Figs 19(d)-(f) show the projections of the ROA on three 2-d planes. These figures also highlight the equilibrium using an asterisk in each of them. The following are the observations and conclusion:

- Figures 19(d), (f) show that the ROA extends over $v_{dc}(0) \in [0.25,\ 2.63]\ kV$. Considering the fact that in a realistic power system the frequency variation practically does not go outside 60 ± 2 Hz, we see the ROA covers well beyond this range. On a similar note, considering the nominal value of $\bar{P}_{\tau gT} = 2{,}450\ MW$, we see from Fig. 19 (e) that for $f_{COI} = 60 \pm 2\ Hz$, the ROA extends to $\underline{P}_{\tau gT}$ values that are $\approx \pm 100\%$ of $\bar{P}_{\tau gT}$.
- Based on these observations we conclude, within the practical range of variation of the state variables associated with (12), the system is asymptotically stable. This shows the applicability and limitation of Lemma V.4

3) Phasor Model of Modified IEEE 16-machine System: The phasor model of 16- machine system, which is shown in Fig. 14, is modified again for class-B GFCs. We remove class-A GFCs and add 6 class-B GFCs at buses 12, 18, 22, 32, 34, and 54, which deliver $\approx 4.6\ GW$, i.e., 25 % of total load.

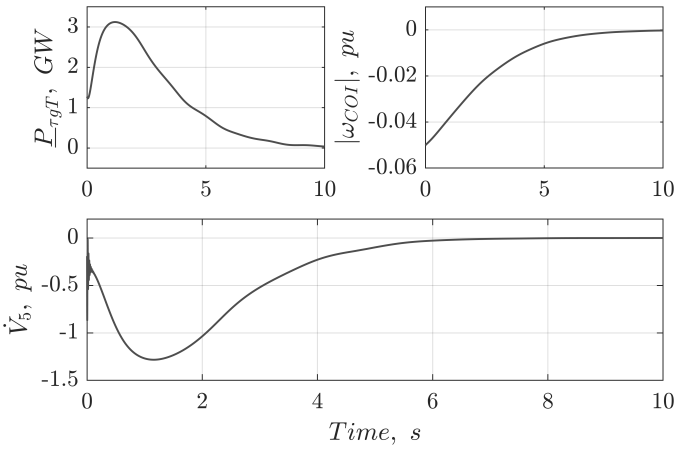

Fig. 20. Unforced response of class-B GFCs in 16-machine system with initial states $P_{\tau gT}(0) = 1.1\bar{P}_{\tau gT}$, and $\omega_g^r(0) = 0.95\bar{\omega}_g^r, \forall r$.

Focusing on Lemma V.4, we performed a multitude of experiments and did find initial states for which the system is unstable. However, we could not perform a design of experiment like the 4-machine system due to a significant number of variables in this case. We report one stable case here due to space constraint. The states are perturbed at $t = 0$ s as follows: $P_{\tau gT}(0) = 1.1\bar{P}_{\tau gT}$, and $\omega_g^r(0) = 0.95\bar{\omega}_g^r, \forall r$. Here, superbars represent the nominal values. As observed in Fig. 20, the system is asymptotically stable in this condition. The

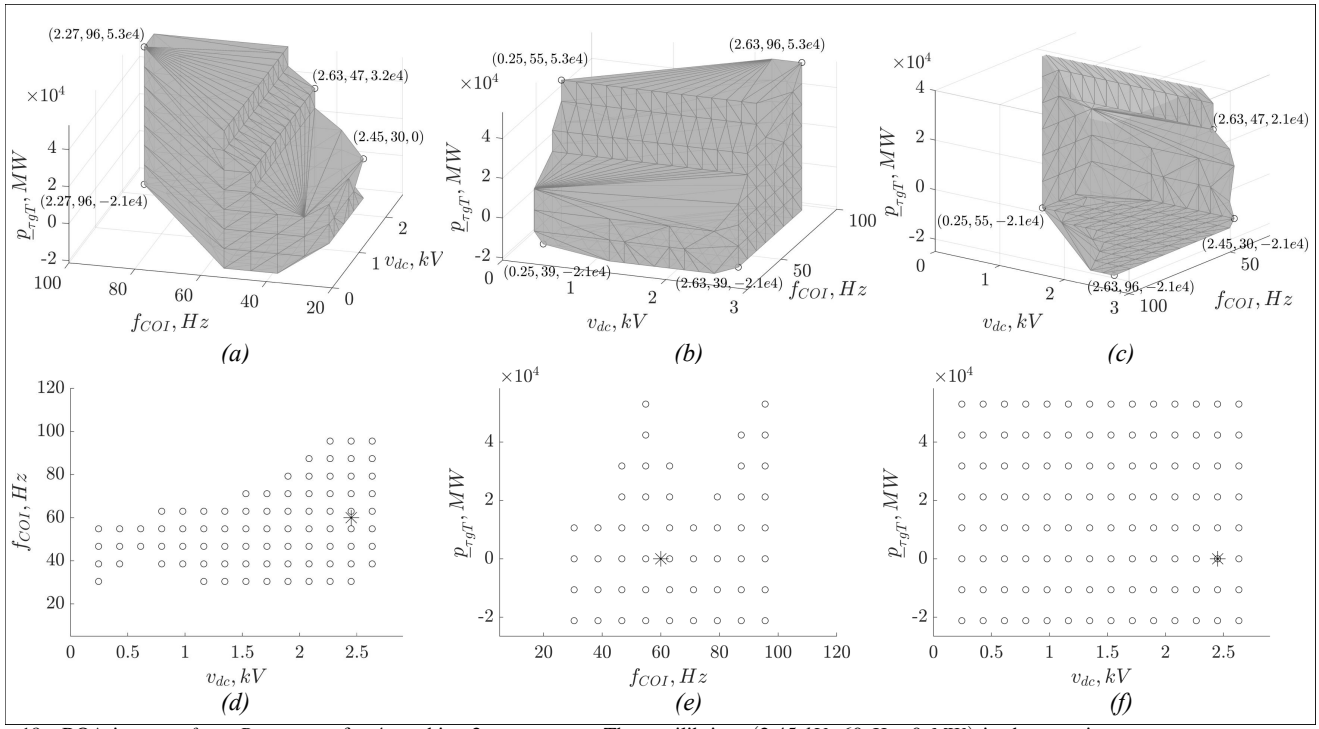

Fig. 19. ROA in $v_{dc} - f_{coi} - \underline{P}_{\tau gT}$ space for 4-machine 2-area system. The equilibrium $(2.45\ kV,\ 60\ Hz,\ 0\ MW)$ is shown using $*$.

Lyapunov function V_5 for unforced system follows (16) whose rate of change along the trajectories of the system is always negative (except at the origin) satisfying the condition for asymptotic stability.

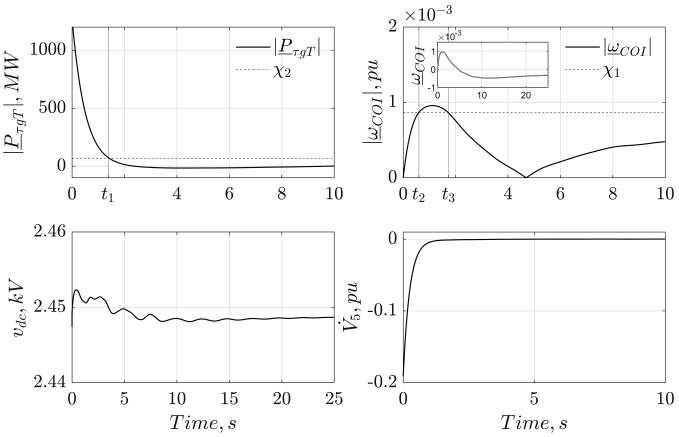

Fig. 21. Response of 16-machine system following a step increased of 62 MW in total load at $t = 0$ s, while at same instant, the initial value of $P_{\tau g}$ is set to 1.1 times the nominal value.

Finally, the input-to-state stability of class-B GFCs in 16-machine system is demonstrated by applying a step increase of 62 MW in load at $t = 0$ s and the state $P_{\tau gT}$ is perturbed to 1.1 times of its nominal value. This load increment is less than $\theta n_1 \underline{P}_c^{max}$, since $0 < \theta < 1$, $n_1 = 6$, and $\underline{P}_c^{max} = 97$ MW. As shown in Fig. 21, the system is stable after the load increase and $\dot{V}_5$ satisfies the sufficiency conditions till $t = t_3$ s. As these constraints derived in Theorem V.5 are conservative, $\dot{V}_5$ is negative (almost zero) even after the conditions are violated.

Remark IV: Based on the results concerning class-B GFCs, we notice that the 'global' nature of asymptotic stability postulated by Lemma V.4 is not true for a detailed system model. This is expected, since the lemma is supposed to hold as long as the assumptions leading to the reduced-order model is valid. Nevertheless, our experiments confirm a significantly large ROA for class-B GFCs around the equilibria we tested with.

C. Results with Generator Trip

In all the previous experiments, we considered step increase in the constant power load of the system. In this section, we consider the tripping of SG4 in the modified IEEE 4-machine 2-area System to validate two of the proposed theorems that are applicable under this condition. In the modified system, SG1, SG4 and the GFC at bus 3 are generating 350 MW, 150 MW, and 350 MW, respectively, the loads have a unity power factor, and the real power load at bus 9 is 1217 MW. Although, the theorems in Section V are validated for a constant power load, the generator tripping in presence of constant power load leads to infeasible load flow condition (i.e., voltage collapse) in this system. Hence, the real power portion of the load is modeled as 50% constant power and 50% constant impedance in the modified 4-machine system. Other parameters and variables of this test system can be found in [15] and in Table V of the Appendix.

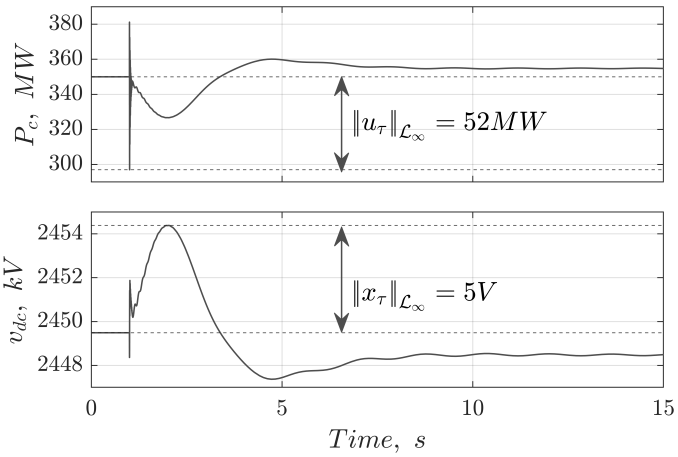

Fig. 22. Plot of P_c and v_{dc} following the trip of SG4 at $t = 1$ s in modified IEEE 4-machine system in presence of class-A GFC.

1) Generator trip in presence of Class-A GFC: A class-A GFC is considered at bus 3 for this case. After SG4 is tripped at $t = 1$ s, the power generation (P_c) from the GFC experiences transients and finally settles at a higher value than the pre-disturbance output as shown in Fig. 22. Here, for the GFC $P_c^{max} = 53$ MW, so $\|u_\tau\|_{\mathcal{L}_p} = 52$ satisfies the the condition $\sup_{0 \le t \le \tau} |u| \le \underline{P}_c^{max}$ as mentioned in Remark I and v_{dc} is found to be stable as described in Theorem V.2. Also, for this case, $|m| = 1.9e3$ $\mho$, $y_m = 2.43$ kV, and $|x_0| = 0$, which gives the bound on the peak deviation of v_{dc} as 11 V. As Fig. 22 shows, the actual value of peak deviation is 5 V, which respects this bound and satisfies the condition $\{|x| \le r\} \subset \tilde{D}_x$.

2) Generator trip in presence of Class-B GFC: For this case, the GFC is operating in class-B control mode keeping all the other parameters the same as in the previous one. After the SG4 trip, in this case, v_{dc} is stable as shown in Fig. 23. As the loading condition doesn't change during this event, this can be treated as an unforced system and the stability condition in Lemma V.4 can be tested for the post-disturbance equilibrium. In Fig. 23, the derivative of the Lyapunov function ($\dot{V}_5$) as derived in (16) is shown along with two states $\underline{\omega}_{COI}$ and $\underline{P}_{\tau g}$. It is found that $\dot{V}_5$ is always negative following the generation loss, and it satisfies the asymptotic stability condition in Lemma V.4.

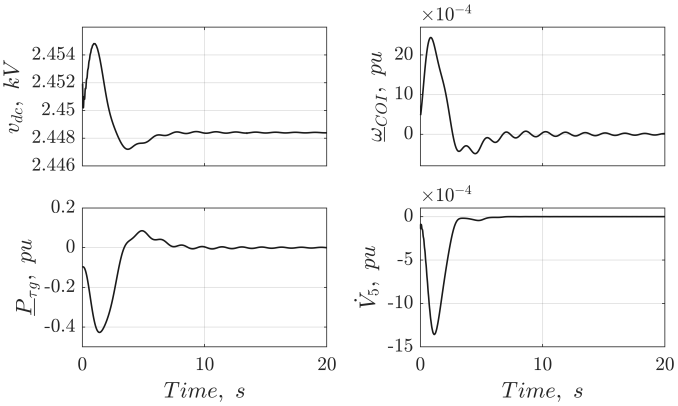

Fig. 23. Response of modified IEEE 4-machine system in presence of class-B GFC after SG4 tripped at $t = 0$ s.

VII. Conclusion

It was shown that for class-A GFCs the stability conditions can be derived by focusing on the dc-link voltage dynamics in isolation, whereas class-B GFCs need to consider system's frequency dynamics as well. The ROA of a class-A GFC was shown to be a subset of its class-B counterpart. Moreover, it was possible to derive sufficiency conditions for small-signal finite gain $\mathcal{L}_p$ stability of class-A GFC, whereas constraints guaranteeing (large-signal) input-to-state state stability of class-B GFC following bounded variations in the load was provided. Therefore, these propositions analytically establish superior stability properties of class-B GFCs in primary frequency response regime. Finally, exhaustive testing through detailed switched models and full-order phasor models indicate that the lemmas and theorems, although established using reduced-order models, largely hold in realistic power systems.

Appendix

TABLE II
Parameters for Standalone class-A GFC

d_{pc}	$1.6e-4\ Hz(kW)^{-1}$	i_{dc}^{max}	$75\ A$	G_c	$0.83e-6\ \mho$
τ_c	$0.001\ s$	ω^*	$314\ rad/s$	k_c	$1.6\ \mho$
P_c^{max}	$178\ kW$	P_c^*	$150\ kW$	v_{dc}^*	$2.44\ kV$

TABLE III
Parameters for each class-A GFC in 16-machine system

d_{pc}	$2.1e-3\ Hz(MW)^{-1}$	i_{dc}^{max}	$440\ kA$	G_c	$0.83\ \mho$
τ_c	$0.001\ s$	ω^*	$377\ rad/s$	k_c	$2e3\ \mho$
P_c^{max}	$1074\ MW$	P_c^*	$976\ MW$	v_{dc}^*	$2.45\ kV$

TABLE IV
Parameters for each class-B GFC in 16-machine system

k_m	$0.0245\ Hz/V$	i_{dc}^{max}	$360\ kA$	k_c	$2e3\mho$
G_c	$0.83\mho$	τ_c	$0.001\ s$	ω^*	$377\ rad/s$
P_c^{max}	$871.3\ MW$	P_c^*	$774.5\ MW$	v_{dc}^*	$2.45\ kV$

Machine and transmission line parameters of 16-machine system are used from [19].

TABLE V
Parameters for GFC in 4-machine system

k_m	$0.0245\ Hz/V$	i_{dc}^{max}	$166\ kA$	k_c	$2e3\mho$
G_c	$0.83\mho$	τ_c	$0.001\ s$	d_{pc}	$2e-3Hw(MW)^{-1}$
P_c^{max}	$402\ MW$	P_c^*	$350\ MW$	v_{dc}^*	$2.45\ kV$

Machine and transmission line parameters of 4-machine system are available in [15].

References

[1] N. W. Miller, M. Shao, S. Pajic, and R. D'Aquila, "Western wind and solar integration study phase 3-frequency response and transient stability," *National Renewable Energy Lab.(NREL), Golden, CO (United States); GE Energy Management, Schenectady, NY (United States), Tech. Rep.*, 2014.

[2] EirGrid and Soni, "DS3: System Services Review TSO Recommendations," *EirGrid, Tech. Rep*, 2012.

[3] F. Milano, F. Dörfler, G. Hug, D. J. Hill, and G. Verbič, "Foundations and challenges of low-inertia systems (invited paper)," in *2018 Power Systems Computation Conference (PSCC)*, 2018, pp. 1–25.

[4] M. C. Chandorkar, D. M. Divan, and R. Adapa, "Control of parallel connected inverters in standalone ac supply systems," *IEEE Transactions on Industry Applications*, vol. 29, no. 1, pp. 136–143, 1993.

[5] Q. Zhong and G. Weiss, "Synchronverters: Inverters that mimic synchronous generators," *IEEE Transactions on Industrial Electronics*, vol. 58, no. 4, pp. 1259–1267, 2011.

[6] G. Seo, M. Colombino, I. Subotic, B. Johnson, D. Groß, and F. Dörfler, "Dispatchable virtual oscillator control for decentralized inverter-dominated power systems: Analysis and experiments," in *2019 IEEE Applied Power Electronics Conference and Exposition (APEC)*, 2019, pp. 561–566.

[7] C. Arghir, T. Jouini, and F. Dörfler, "Grid-forming control for power converters based on matching of synchronous machines," *Automatica*, vol. 95, pp. 273–282, 2018, ISSN: 0005-1098.

[8] S. Samanta and N. R. Chaudhuri, "On stability analysis of power grids with synchronous generators and grid-forming converters under dc-side current limitation," in *2021 American Control Conference (ACC)*. arXiv: 2103.09966 [cs.SY].

[9] A. Tayyebi, D. Groß, A. Anta, F. Kupzog, and F. Dörfler, "Frequency stability of synchronous machines and grid-forming power converters," *IEEE Journal of Emerging and Selected Topics in Power Electronics*, vol. 8, no. 2, pp. 1004–1018, 2020.

[10] U. Markovic, O. Stanojev, P. Aristidou, E. Vrettos, D. Callaway, and G. Hug, "Understanding small-signal stability of low-inertia systems," *IEEE Transactions on Power Systems*, vol. 36, no. 5, pp. 3997–4017, 2021.

[11] Y. Gao, H.-P. Ren, and J. Li, *Grid-forming converters control based on dc voltage feedback*, 2020. arXiv: 2009.05759 [eess.SY].

[12] A. Tayyebi, A. Anta, and F. Dörfler, *Hybrid angle control and almost global stability of grid-forming power converters*, 2020. arXiv: 2008.07661 [math.OC].

[13] S. Curi, D. Groß, and F. Dörfler, "Control of low-inertia power grids: A model reduction approach," in *2017 IEEE 56th Annual Conference on Decision and Control (CDC)*, 2017, pp. 5708–5713.

[14] P. Sauer and M. Pai, *Power System Dynamics and Stability*. Prentice Hall, 1998.

[15] P. Kundur, N. Balu, and M. Lauby, *Power System Stability and Control*, ser. EPRI power system engineering series. McGraw-Hill Education, 1994.

[16] H. Ghaffarzadeh and A. Mehrizi-Sani, "Review of control techniques for wind energy systems," *Energies*, 2020. [Online]. Available: https://www.mdpi.com/1996-1073/13/24/6666.

[17] H. K. Khalil, *Nonlinear systems; 3rd ed.* Prentice-Hall, 2002.

[18] A. Tayyebi, D. Groß and A. Anta, *Grid forming converters: Implementation of grid-forming control techniques in IEEE 9-bus system*, https://github.com/ATayebi/GridFormingConverters, 2019.

[19] N. R. Chaudhuri, "Wide-area Monitoring and Control of Future Smart Grids," Ph.D. dissertation, Imperial College, London, U.K., Jun. 2011.

[20] PSCAD/EMTDC, *Manitoba HVDC Research Centre*, version 4.6. [Online]. Available: https://www.pscad.com.

[21] *MATLAB version 9.8.0.1396136 (R2020a)*, The Mathworks, Inc., Natick, Massachusetts, 2020.

Sayan Samanta (S'19) received his B.Tech and M.Tech degree in Electrical Engineering from Indian Institute of Technology (IIT) Kharagpur, India, in 2019. Currently, he is pursuing his Ph.D. in Electrical Engineering at The Pennsylvania State University, USA. His research interests include modeling and control of large power systems in presence of converters and synchronous machines.

Nilanjan Ray Chaudhuri (S'08-M'09-SM'16) received the Ph.D. degree in power systems from Imperial College London, London, UK in 2011. From 2005 to 2007, he worked in General Electric (GE) John F. Welch Technology Center. He came back to GE and worked in GE Global Research Center, NY, USA as a Lead Engineer during 2011 to 2014. Presently, he is an Associate Professor with the School of Electrical Engineering and Computer Science at Penn State, University Park, PA. He was an Assistant Professor with North Dakota State University, Fargo, ND, USA during 2014-2016. He is a member of the IEEE and IEEE PES. Dr. Ray Chaudhuri is the lead author of the book Multi-terminal Direct Current Grids: Modeling, Analysis, and Control (Wiley/IEEE Press, 2014). He served as an Associate Editor of the IEEE TRANSACTIONS ON POWER DELIVERY (2013 – 2019) and IEEE PES LETTERS (2016 - present). Dr. Ray Chaudhuri was the recipient of the National Science Foundation Early Faculty CAREER Award in 2016 and Joel and Ruth Spira Excellence in Teaching Award in 2019.